City, University of London Institutional Repository

Reuleaux plasticity: Analytical backward Euler stress integration and consistent tangent

William M. Coombs, Roger S. Crouch *, Charles E. Augarde

School of Engineering and Computing Sciences, Durham University, South Road, Durham, DH1 3LE, United Kingdom

ABSTRACT

Analytical backward Euler stress integration is presented for a deviatoric yielding criterion based on a modified Reuleaux triangle. The criterion is applied to a cone model which allows control over the shape of the deviatoric section, independent of the internal friction angle on the compression meridian. The return strategy and consistent tangent are fully defined for all three regions of principal stress space in which elastic trial states may lie. Errors associated with the integration scheme are reported. These are shown to be less than 3% for the case examined. Run time analysis reveals a 2.5–5.0 times speed-up (at a material point) over the iterative Newton–Raphson backward Euler stress return scheme. Two finite-element analyses are presented demonstrating the speed benefits of adopting this new formulation in larger boundary value problems. The simple modified Reuleaux surface provides an advance over Mohr–Coulomb and Drucker–Prager yield envelopes in that it incorporates dependencies on both the Lode angle and intermediate principal stress, without incurring the run time penalties of more sophisticated models.

1. Introduction

While a vast body of constitutive models has been generated over the last decades, very few of the advanced formulations have gained widespread use. This has been largely a consequence of their computational burden. Developing algorithmically efficient and fully robust constitutive models for engineering materials has therefore become just as important as providing realism, in order to allow detailed three dimensional non-linear deformation analyses to be undertaken.

In this paper we offer a simple cone-type (frictional) elasto-plastic formulation, which allows an analytical backward Euler (BE) stress integration on the curved surface and exact integration in the regions where singularities appear. The BE scheme gives a fully implicit approximation. The popularity of this approach over explicit schemes (for example [15]) is due to its high level of accuracy for a given numerical effort, particularly when large strain increments are applied [13]. The associated perfect plasticity model presented here may be thought of as a simple hybrid sitting between the Drucker–Prager (D–P) and Mohr–Coulomb (M–C) formulations. The D–P yield surface exhibits no Lode angle dependency, θ. The M–C surface has no sensitivity to the intermediate principal stress, σ_2. Yet multiaxial experiments show that both factors influence yielding and peak stress. Their inclusion in constitutive models appears necessary in order to capture the deformation of geotechnical structures [2]. The attraction of the

proposed model is the improved fit to deviatoric yielding (the formulation has a sensitivity to θ and σ_2) and a one-step integration scheme. The consequences of neglecting Lode angle and σ_2 dependencies are discussed further in Section 2.

The layout of the paper is as follows. In Section 2 the particular form of the deviatoric section is introduced. Section 3 describes the stress return strategies for the three regions where the elastic trial stress may lie. The approach, when returning to the compression meridian or tensile apex, follows Clausen et al.'s method [4]. When returning elsewhere, finding the closest point to the surface in energy-mapped space [5] requires the solution of a quartic. Section 3 also gives the consistent tangent expressions for each region and quantifies the errors associated with the analytical stress return. Section 4 presents a run time comparison between the standard iterative BE stress return and the proposed analytical single-step return. Two finite-element simulations are presented in Section 5. The analysis of a single 3D finite-element toy problem illustrates the asymptotic quadratic convergence of the global Newton–Raphson (N–R) solution scheme. A larger, rigid footing plane-strain finite-element, analysis compares solutions obtained from the proposed model with those obtained from D–P, M–C and Willam–Warnke (W–W [16]) cones. A number of other forms of Lode angle dependencies on the yield surface have been proposed in the literature [1,3,10,17]. These can improve on the relatively poor fit of the D–P and M–C idealisations, yet none offer the advantage of a closed form BE integration solution which is available for the formulation proposed here.

In all that follows $\{\cdot\}$ and $[\cdot]$ denote vectors and matrices respectively, $\hat{(\cdot)}$ and $\overline{(\cdot)}$ identify terms associated with principal and shear components of generalised stiffness matrices and $\{\cdot\}^T$ denotes a
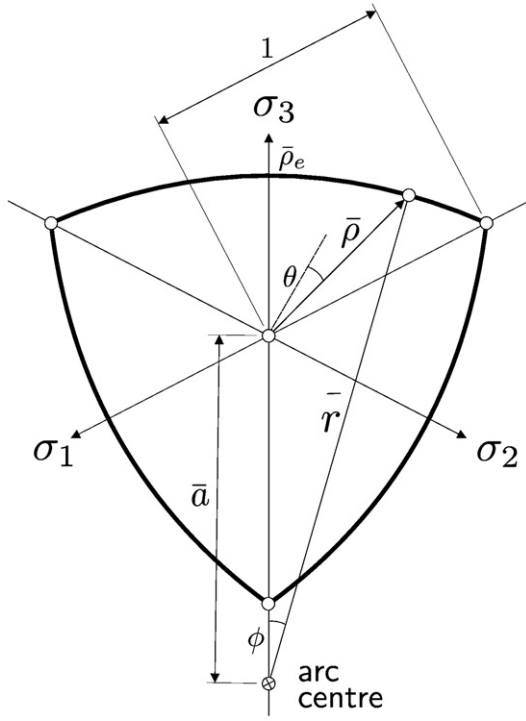
Fig. 1. Modified Reuleaux triangle definition.

vector transpose. We adopt a tension positive convention and assume the following ordering of the principal stresses $\sigma_1 \leq \sigma_2 \leq \sigma_3$.

2. Modified Reuleaux

For the plasticity models under consideration, the yield surfaces may be defined using Haigh–Westergaard cylindrical coordinates ξ, ρ and θ. The normalised deviatoric radius, $\bar{\rho} = \rho/\rho_c$, is employed; where ρ_c is the radius on the compression meridian ($\theta = \pi/6$) and ρ is a function of the Lode angle $\theta \in [-\pi/6, \pi/6]$

$$\theta = \frac{1}{3} \arcsin\left(\frac{-3\sqrt{3}}{2} \frac{J_3}{J_2^{3/2}} \right). \tag{1}$$

Here $J_2 = (\text{tr}[s]^2)/2, J_3 = (\text{tr}[s]^3)/3, [s] = [\sigma] - \xi[1]/\sqrt{3}, \xi = \text{tr}[\sigma]/\sqrt{3}$ and [1] denotes the third-order identity matrix.

From geometric considerations (see Fig. 1) the modified Reuleaux (MR) Lode angle dependency may be obtained as

$$\bar{\rho}(\theta) = \sqrt{\bar{a}^2 + \bar{r}^2 - 2\bar{a}\,\bar{r}\cos(\phi)}, \tag{2}$$

where

$$\bar{r} = \frac{\bar{\rho}_e^2 - \bar{\rho}_e + 1}{2\bar{\rho}_e - 1}, \; \bar{a} = \bar{r} - \bar{\rho}_e \text{ and } \bar{\rho}_e = \frac{\rho_e}{\rho_c}. \tag{3}$$

$\bar{\rho}_e \in [0.5,1]$ gives the relative size of the radius under triaxial extension ($\sigma_1 = \sigma_2 < \sigma_3$) with respect to that under triaxial compression ($\sigma_1 < \sigma_2 = \sigma_3$). The arc angle, ϕ, is defined as

$$\phi = \frac{\pi}{6} + \theta - \arcsin\left(\frac{\bar{a}\sin(5\pi/6 - \theta)}{\bar{r}} \right). \tag{4}$$

If the arc centres coincide with the singularities on the compression meridians (that is, if $\bar{r} = 1 + \bar{\rho}_e$ so that $\bar{a} = 1$) then the shape of the deviatoric section is a Reuleaux triangle. Although this shape was used in cam-actuated steam engine regulators in the 1830s, the first written discussion of the geometry appears to have been provided by Franz Reuleaux in 1876, when considering a family of curved shapes of constant breadth (that is, rolling polygons which maintain a constant height) [9,11]. Allowing the location of the arc centres to vary along projections of the compression meridians gives rise to the *modified Reuleaux triangle*. As $\bar{\rho}_e \to 0.5$ both $\bar{r}$ and $\bar{a}$ tend to ∞ and the deviatoric section becomes an equilateral triangle. If $\bar{\rho}_e = 1$ then $\bar{\rho} = 1$ and we recover a circular deviatoric section centred on the hydrostatic axis (as found in the D–P model).

Fig. 2 compares the proposed deviatoric section with those attributed to M–C, W–W and Bhowmik–Long (B–L, [3], with a normalised deviatoric radius of $\bar{\rho}_s = 0.73$ on the shear meridian, $\theta = 0$) for $\bar{\rho}_e = 0.656$. The multiaxial experimental data on Monterey sand [8] shown in the figure indicate that this material has both a Lode angle dependency (Fig. 2(A)) and a sensitivity to the intermediate principal stress (Fig. 2(B)). Unlike the other models mentioned above, a D–P surface provides no variation in $\bar{\rho}$ with respect to θ ($\bar{\rho}$ would
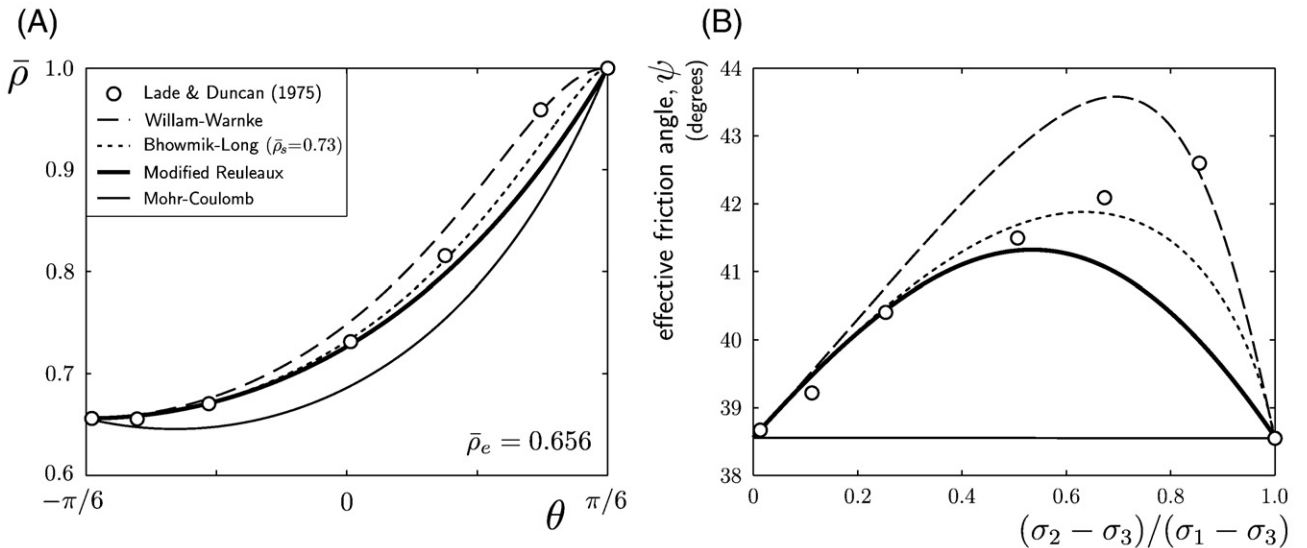

Fig. 2. Modified Reuleaux deviatoric function compared with other functions and experimental data from Lade and Duncan [8]: (A) Lode angle dependency and (B) intermediate principal stress dependency.

equal 1 in Fig. 2(A)). The effective friction angle in Fig. 2(B) is calculated from the expression given by Griffiths

$$\psi = \arcsin\left(\frac{\sqrt{3}\eta\cos(\theta)}{\sqrt{2}+\eta\sin(\theta)}\right), \tag{5}$$

where $\eta=\rho/\xi$ [7]. In that Figure, the M–C envelope exhibits no sensitivity to σ_2. It is evident that the proposed MR deviatoric section offers an improved fit over the D–P and M–C surfaces while maintaining a relatively simple mathematical form. Although the W–W and B–L envelopes provide more satisfactory fits to the experimental data when the intermediate stress ratio $0.5<b<0.95$ (where $b=(\sigma_2-\sigma_3)/(\sigma_1-\sigma_3)$), neither the W–W nor the B–L model are able to offer analytical BE stress integration solutions for arbitrary strain increments. Thus they can incur significant computational overheads (compared with D–P and M–C models) when introduced into a large-scale elasto-plastic stress analysis. It is worth adding that a number of geotechnical problems satisfy plane-strain conditions, where b typically lies close to 0.3 [12]. The MR solution provides a good fit to the multiaxial data in this region.

The MR cone can be defined as

$$f(\eta,\theta) = \alpha\bar{\rho}-\eta = 0 \tag{6}$$

where α is the opening angle of the cone, $\alpha=-\tan(\psi_{MC})$. ψ_{MC} is the M–C internal friction angle of the material under triaxial compression. Thus Eq. (6) defines a cone with a MR deviatoric section and linear meridians, pinned at the stress origin with the space diagonal $(\sigma_1=\sigma_2=\sigma_3)$ as the cone's axis, see Fig. 3. The MR cone can be seen as a hybrid surface, lying between the D–P and M–C envelopes, allowing some control over the shape of the deviatoric section, independent of the cone opening angle.

3. Stress return and consistent tangent

Consider the trial elastic stress $\{\sigma_t\}$ (given by a trial elastic strain $\{\varepsilon_t^e\}$) lying outside the yield surface ($f > 0$). For this state there are three distinct stress return regions associated with the MR cone, as shown in Fig. 3, namely:

A. Return to the stress origin (point),
B. return to the compression meridian (line),
C. return to the non-planar surface.

The Closest Point Projection (CPP) and consistent tangent are considered for each region in Sections 2–4. Table 1 gives the pseudo-code for the stress return algorithm.
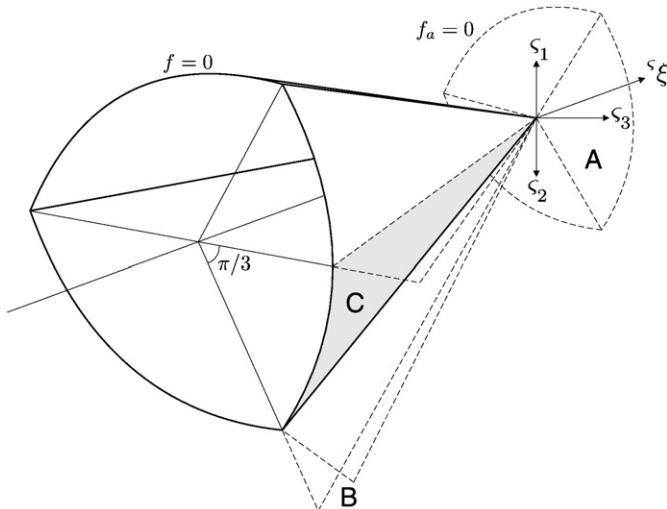

Fig. 3. Modified Reuleaux cone stress return regions.

3.1. Energy-mapped stress space

Simo and Hughes [13] showed that the BE integration corresponds to the minimisation of

$$\{\{\sigma_r\}-\{\sigma_t\}\}^T[C^e]\{\{\sigma_r\}-\{\sigma_t\}\}, \tag{7}$$

with respect to the return stress $\{\sigma_r\}$ (where $[C^e]$ is the elastic compliance matrix), which represents a CPP. The minimisation is subject to the following constraints

$$f \leq 0, \; \dot{\gamma} \geq 0, \; f\dot{\gamma} = 0. \tag{8}$$

$(\cdot)_t$ and $(\cdot)_r$ denote quantities associated with the trial state and the return state respectively, where f is the yield function and $\dot{\gamma}$ is the plastic multiplier. The return stress is not generally the closest point geometrically in standard stress space, but rather the stress that minimises the energy square norm Eq. (7). In this paper we make use of energy-mapped $\{\varsigma\}$ space [5], where

$$\frac{1}{E}\{\varsigma\}^T\{\varsigma\} = \{\sigma\}^T[C^e]\{\sigma\}, \tag{9}$$

and E is the Young's modulus of the elastically isotropic material. This allows us to find the geometric closest point (in $\{\varsigma\}$ space) through use of the following transformation

$$\{\varsigma\} = [T]\{\sigma\}. \tag{10}$$

For isotropic linear elasticity, $[T]$ is solely a function of Poisson's ratio υ. Given the elastic compliance matrix

$$[C^e] = \frac{1}{E}\begin{bmatrix} 1 & -\upsilon & -\upsilon & 0 & 0 & 0 \\ -\upsilon & 1 & -\upsilon & 0 & 0 & 0 \\ -\upsilon & -\upsilon & 1 & 0 & 0 & 0 \\ 0 & 0 & 0 & 2(1+\upsilon) & 0 & 0 \\ 0 & 0 & 0 & 0 & 2(1+\upsilon) & 0 \\ 0 & 0 & 0 & 0 & 0 & 2(1+\upsilon) \end{bmatrix}, \tag{11}$$

$[T]$ becomes

$$[T] = \begin{bmatrix} t_1 & t_2 & t_2 & 0 & 0 & 0 \\ t_2 & t_1 & t_2 & 0 & 0 & 0 \\ t_2 & t_2 & t_1 & 0 & 0 & 0 \\ 0 & 0 & 0 & t_3 & 0 & 0 \\ 0 & 0 & 0 & 0 & t_3 & 0 \\ 0 & 0 & 0 & 0 & 0 & t_3 \end{bmatrix}, \tag{12}$$

where

$$t_1 = \frac{\sqrt{1-2\upsilon}+2\sqrt{1+\upsilon}}{3}, \; t_2 = \frac{\sqrt{1-2\upsilon}-\sqrt{1+\upsilon}}{3}, \; t_3 = \sqrt{2(1+\upsilon)}. \tag{13}$$

This mapping leads to a squashing and a stretching of the yield surface in the hydrostatic and deviatoric directions respectively (see Fig. 4).

$$^\varsigma\xi = \xi\sqrt{1-2\upsilon}, \; ^\varsigma\rho = \rho\sqrt{1+\upsilon}, \; ^\varsigma\theta = \theta, \tag{14}$$

where $^\varsigma(\cdot)$ denotes a quantity associated with energy-mapped space. The energy-mapped opening angle of the cone, $^\varsigma\alpha$, is

$$^\varsigma\alpha = \frac{\alpha\sqrt{1+\upsilon}}{\sqrt{1-2\upsilon}}. \tag{15}$$

Once the closest point solution in energy-mapped stress space has been found, the solution can be transformed back to conventional stress space. Note that we need only operate with principal stresses (conventional and energy-mapped) in the solution process for an isotropic model.
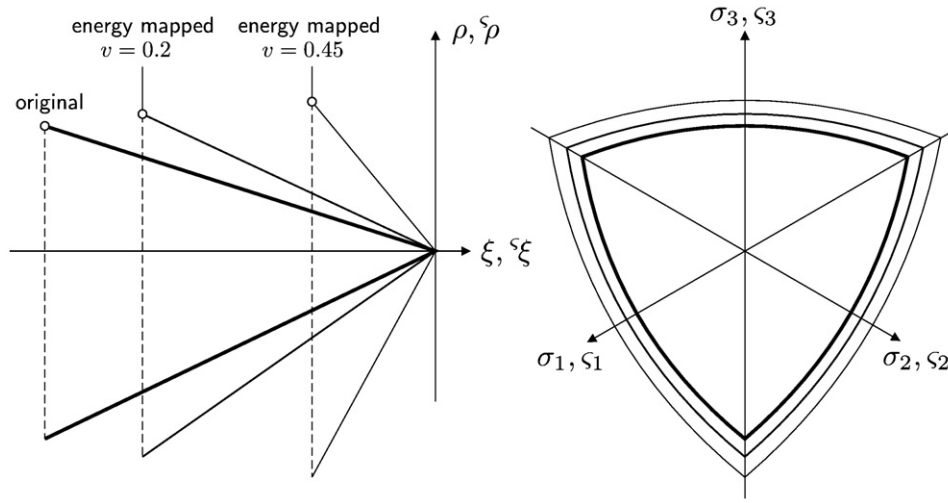
Fig. 4. Modified Reuleaux cone energy-mapped $\{\varsigma\}$ space transformation.

3.2. Stress origin return

If $f_a<0$ then the trial stress point $\{\varsigma_t\}$ will be returned onto the apex of the MR cone, with

$$\{\varsigma_{cp}\} = \{\sigma_{cp}\} = \{0\}, \tag{16}$$

where $(\cdot)_{cp}$ denotes quantities associated with the closest point. The apex yield function is given by

$$f_a = \frac{\bar{\rho}}{\varsigma_\alpha} + {}^\varsigma\eta = 0. \tag{17}$$

3.2.1. Stress origin consistent tangent

As Clausen et al. [4] have shown, the elasto-plastic consistent tangent for a hydrostatic apex return is simply given by

$$[D^{alg}] = [0]. \tag{18}$$

3.3. Compression meridian return

The trial arc angle ϕ_t should be checked against ϕ_{cr} to determine if the trial point returns onto the compression meridian, where

$$\phi_{cr} = \arcsin\left(\frac{\sqrt{3}}{2\bar{r}}\right). \tag{19}$$

If $\phi_t \geq \phi_{cr}$ then

$$\theta_{cp} = \pi/6, \; {}^\varsigma\rho_{cp} = {}^\varsigma\alpha^\varsigma\xi_{cp}.$$

One obtains the solution for this case by considering a plane normal to the compression meridian of the energy-mapped yield surface. The closest point and trial point will lie in the same normal plane. We make use of

$$\{{}^\varsigma n\}^T \{\{\varsigma_{cp}\} - \{\varsigma_t\}\} = 0 \tag{20}$$

where $\{{}^\varsigma n\}$ is the normal to the plane; which in this case is the vector defining the corner line of the energy-mapped yield surface. $\{{}^\varsigma n\}$ is given by

$$\{{}^\varsigma n\} = \left\{1 - \sqrt{2}{}^\varsigma\alpha \quad 1 + {}^\varsigma\alpha/\sqrt{2} \quad 1 + {}^\varsigma\alpha/\sqrt{2}\right\}^T, \tag{21}$$

and any $\{\varsigma\}$ on this line is given by

$$\{\varsigma\} = \frac{{}^\varsigma\xi}{\sqrt{3}}\left\{1 - \sqrt{2}{}^\varsigma\alpha \quad 1 + {}^\varsigma\alpha/\sqrt{2} \quad 1 + {}^\varsigma\alpha/\sqrt{2}\right\}^T. \tag{22}$$

Substituting Eqs. (21) and (22) into Eq. (20) we obtain an equation which can be solved for ${}^\varsigma\xi_{cp}$

$$
{}^\varsigma\xi_{cp} = \frac{\left(\varsigma_{t_2} + \varsigma_{t_3}\right)\left(1 + {}^\varsigma\alpha/\sqrt{2}\right) + \varsigma_{t_1}\left(1 - \sqrt{2}{}^\varsigma\alpha\right)}{\sqrt{3}(1 + {}^\varsigma\alpha^2)} \tag{23}
$$

Subsequently ${}^\varsigma\xi_{cp}$ and ${}^\varsigma\rho_{cp}$ can be transformed back into conventional stress space to calculate the final return stress $\{\sigma_{cp}\}$ using the Haigh–Westergaard solution

$$\{\sigma\} = \frac{\xi}{\sqrt{3}}\{1\} + \sqrt{\frac{2}{3}}\rho\{\sin(\theta - 2\pi/3) \quad \sin(\theta) \quad \sin(\theta + 2\pi/3)\}^T \tag{24}$$

where $\{1\} = \{1\;1\;1\}^T$. These stresses are then transformed back from principal to generalised stress space through use of the eigenvectors associated with the generalised trial stress state.

3.3.1. Compression meridian consistent tangent

The consistent tangent for a corner return is obtained following the approach given by Clausen et al. [4]. By considering the vector orientation of the edge

$$\{n\} = \left\{1 - \sqrt{2}\alpha \quad 1 + \alpha/\sqrt{2} \quad 1 + \alpha/\sqrt{2}\right\}^T \tag{25}$$

we obtain the third-order elasto-plastic tangent matrix (in principal form) as

$$\left[\hat{D}^{ep}\right] = \frac{\{n\}\{n\}^T}{\{n\}^T[\hat{C}^e]\{n\}} \tag{26}$$

where $[\hat{C}^e]$ is the third-order (principal) elastic compliance matrix. The generalised (sixth-order) elasto-plastic tangent matrix is then given by

$$[D^{ep}] = \begin{bmatrix} [\hat{D}^{ep}] & [0] \\ [0] & (E/2(1+\upsilon))[1] \end{bmatrix} \tag{27}$$

The consistent tangent follows as

$$[D^{alg}] = [Q][D^{ep}],\qquad(28)$$

where $[Q]$ is calculated from

$$[Q] = \left([I] + \Delta\gamma[C^e]^{-1}\left[\frac{\partial^2 f}{\partial\sigma_{cp}^2}\right]\right)^{-1},\qquad(29)$$

where $[I]$ is the sixth-order identity matrix [4]. In principal stress space $[Q]$ can be calculated as

$$[Q] = \begin{bmatrix} [1] & [0] \\ [0] & [\overline{Q}] \end{bmatrix},\qquad(30)$$

where

$$[\overline{Q}] = \begin{bmatrix} 1 + \dfrac{\Delta\sigma_1^p - \Delta\sigma_2^p}{\sigma_1 - \sigma_2} & 0 & 0 \\ 0 & 1 + \dfrac{\Delta\sigma_2^p - \Delta\sigma_3^p}{\sigma_2 - \sigma_3} & 0 \\ 0 & 0 & 1 + \dfrac{\Delta\sigma_1^p - \Delta\sigma_3^p}{\sigma_1 - \sigma_3} \end{bmatrix}^{-1}\qquad(31)$$

$\{\Delta\sigma^p\} = \Delta\gamma[C^e]^{-1}\{f_{,\sigma}\} = \{\sigma_t\} - \{\sigma_{cp}\}$ is the plastic stress corrector increment associated with the return path. Using the fact that $\sigma_2 = \sigma_3$ for a return onto the corner, $[\overline{Q}]$ can be simplified to

$$[\overline{Q}] = \begin{bmatrix} \dfrac{\sigma_1 - \sigma_2}{\sigma_{t_1} - \sigma_{t_2}} & 0 & 0 \\ 0 & 0 & 0 \\ 0 & 0 & \dfrac{\sigma_1 - \sigma_3}{\sigma_{t_1} - \sigma_{t_3}} \end{bmatrix},\qquad(32)$$

where σ_{t_i} are the principal trial stresses. From Eqs. (28) and (32) the consistent tangent, for the line return, can be written as

$$[D^{alg}] = \begin{bmatrix} [\hat{D}^{ep}] & [0] \\ [0] & (E/2(1+v))[\overline{Q}] \end{bmatrix}.\qquad(33)$$

Once the consistent tangent has been formed in principal stress space (Eq. (33)) it must be transformed back to generalised stress space, see Clausen et al. for more details [4].

3.4. Non-planar surface return

If we consider an elastic trial stress $\{\varsigma_t\}$, outside the yield surface, returning onto the non-singular portion of the surface, we can define a length l as the distance between that trial point and a point on the surface at the same φ_t in any deviatoric plane at a given $^\varsigma\xi$ (see Fig. 5)

$$l^2 = (r_t - r)^2 + (^\varsigma\xi - ^\varsigma\xi_t)^2,\qquad(34)$$

where $r = \overline{r}\,^\varsigma\alpha\,^\varsigma\xi$. The deviatoric distance of the trial point from the arc axis is given by

$$r_t^2 = a^2 + {}^\varsigma\rho_t^2 - 2a\,^\varsigma\rho_t\cos\left(\frac{5\pi}{6} - \theta_t\right),\qquad(35)$$

where $a = \overline{a}\,^\varsigma\alpha\,^\varsigma\xi$. Substituting Eqs. (35) and (3) into Eq. (34), we obtain

$$l = \sqrt{B_1{}^\varsigma\xi^2 - 2^\varsigma\xi(^\varsigma\xi_t + B_2 + \overline{r}\,^\varsigma\alpha r_t) + {}^\varsigma\xi_t^2 + {}^\varsigma\rho_t^2},\qquad(36)$$

where

$$B_1 = \overline{a}^{2\varsigma}\alpha^2 + \overline{r}^{2\varsigma}\alpha^2 + 1, \qquad B_2 = \overline{a}\,^\varsigma\alpha\,^\varsigma\rho_t\cos\left(\frac{5\pi}{6} - \theta_t\right).\qquad(37)$$
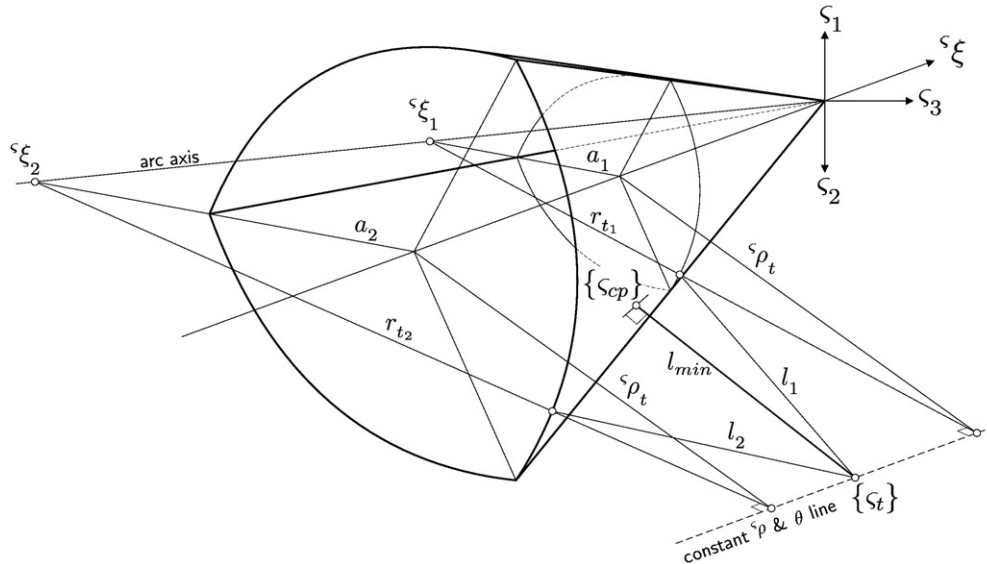

Fig. 5. Geometric solution in energy-mapped $\{\varsigma\}$ space for the surface stress return.

Equating the partial derivative of Eq. (36) with respect to $^{\varsigma}\xi$ to zero, we obtain the closest point on the MR cone to the trial point in $\{\varsigma\}$ space

$$^{\varsigma}\xi_{cp}^4 A_1 + {}^{\varsigma}\xi_{cp}^3 A_2 + {}^{\varsigma}\xi_{cp}^2 A_3 + {}^{\varsigma}\xi_{cp} A_4 + A_5 = 0, \tag{38}$$

where

$$
\begin{aligned}
A_1 &= \bar{a}^{2\varsigma}\alpha^2 B_1^2 - 4\,\bar{a}^4 \bar{r}^{2\varsigma}\alpha^6, \\
A_2 &= 12\,\bar{a}^2 \bar{r}^{2\varsigma}\alpha^4 B_2 - 2\bar{a}^{2\varsigma}\alpha^2 B_1(^{\varsigma}\xi_t + B_2) - 2B_1^2 B_2, \\
A_3 &= \bar{a}^2\alpha^2(^{\varsigma}\xi_t + B_2)^2 + B_1^2\rho_t^2 + 4B_1 B_2(^{\varsigma}\xi_t + B_2) - 9\bar{r}^{2\varsigma}\alpha^2 B_2^2 - 4\bar{a}^2 \bar{r}^{2\varsigma}\alpha^{4\varsigma}\rho_t^2, \\
A_4 &= 6\bar{r}^{2\varsigma}\alpha^{2\varsigma}\rho_t^2 B_2 - 2B_1(^{\varsigma}\xi_t + B_2)^{\varsigma}\rho_t^2 - 2B_2(^{\varsigma}\xi_t + B_2)^2, \\
A_5 &= {}^{\varsigma}\rho_t^2(^{\varsigma}\xi_t + B_2)^2 - {}^{\varsigma}\rho_t^4 \bar{r}^{2\varsigma}\alpha^2.
\end{aligned}
\tag{39}
$$

This quartic can be solved for $^{\varsigma}\xi_{cp}$, see Simo and Hughes page 138 [13], amongst others, for more details. Once $^{\varsigma}\xi_{cp}$ is known, then the other quantities identifying the position of the closest point on the MR surface can be calculated (Fig. 6). ϕ_{cp} is given by the sine rule

$$\phi_{cp} = \arcsin\left(\frac{^{\varsigma}\rho_t \sin(5\pi/6 - \theta_t)}{r_t}\right), \tag{40}$$

where r_t is calculated at the solution $^{\varsigma}\xi_{cp}$ using Eq. (35). $^{\varsigma}\rho_{cp}$ is given by Eq. (2) and θ_{cp} is determined from the cosine rule

$$\theta_{cp} = \frac{5\pi}{6} - \arccos\left(\frac{a_{cp}^2 + {}^{\varsigma}\rho_{cp}^2 - r_{cp}^2}{2a_{cp}^{\varsigma}\rho_{cp}}\right), \tag{41}$$

where r_{cp} and a_{cp} are values associated with $^{\varsigma}\xi_{cp}$.

3.4.1. Non-planar consistent tangent

The consistent tangent for the surface return is calculated by minimising

$$\left\{ \begin{array}{c} \{\varepsilon^e\} - \{\varepsilon_t^e\} + \Delta\gamma\{f_{,\sigma}\} \\ f \end{array} \right\} = \left\{ \begin{array}{c} \{0\} \\ 0 \end{array} \right\}, \tag{42}$$

Fig. 6. Modified Reuleaux closest point in a deviatoric plane.

with respect to $\{\varepsilon_t^e\}$, thereby obtaining

$$\left[\begin{array}{cc} [C^e] + \Delta\gamma[f_{,\sigma\sigma}] & \{f_{,\sigma}\} \\ \{f_{,\sigma}\}^T & 0 \end{array} \right] \left\{ \begin{array}{c} \{d\sigma\} \\ d\Delta\gamma \end{array} \right\} = \left\{ \begin{array}{c} \{d\varepsilon_t^e\} \\ 0 \end{array} \right\}. \tag{43}$$

Rearranging we have

$$\left\{ \begin{array}{c} \{d\sigma\} \\ d\Delta\gamma \end{array} \right\} = \left[\begin{array}{cc} [D^{alg}] & \{D_{12}\} \\ \{D_{21}\} & D_{22} \end{array} \right] \left\{ \begin{array}{c} \{d\varepsilon_t^e\} \\ 0 \end{array} \right\}, \tag{44}$$

where $(\cdot)_{,\sigma}$ and $(\cdot)_{,\sigma\sigma}$, in Eqs. (42) and (43), denote the first and second partial derivatives of $(\cdot)$ with respect to $\{\sigma\}$. Recalling Eq. (6), the first derivative of f with respect to $\{\sigma\}$ is given by

$$\{f_{,\sigma}\} = \alpha\{\bar{\rho}_{,\sigma}\} - \{\eta_{,\sigma}\}, \tag{45}$$

where

$$\{\eta_{,\sigma}\} = \frac{\{\rho_{,\sigma}\}\xi - \rho\{\xi_{,\sigma}\}}{\xi^2}. \tag{46}$$

Operating only with the derivatives with respect to the principal stresses, we obtain

$$\{\rho_{,\sigma}\} = \{s\}/\rho, \qquad \{\xi_{,\sigma}\} = \{1\}/\sqrt{3}. \tag{47}$$

The derivative of $\bar{\rho}$ with respect to $\{\sigma\}$ is given by

$$\{\bar{\rho}_{,\sigma}\} = \bar{\rho}_{,\bar{\rho}\bar{\rho}}\,\bar{\rho}^2_{,\phi}\,\phi_{,\theta}\{\theta_{,\sigma}\}, \tag{48}$$

where

$$\bar{\rho}_{,\bar{\rho}\bar{\rho}} = \frac{1}{2\bar{\rho}}, \qquad \bar{\rho}^2_{,\phi} = 2\bar{a}\,\bar{r}\sin\phi, \qquad \phi_{,\theta} = 1 + \frac{\bar{a}\cos(5\pi/6 - \theta)}{\bar{r}\sqrt{1 - (\bar{a}\sin(5\pi/6 - \theta)/\bar{r})^2}}, \tag{49}$$

$$\{\theta_{,\sigma}\} = \frac{-\sqrt{3}}{2\cos 3\theta}\underbrace{\left(J_2^{-3/2}\{J_{3,\sigma}\} - \frac{3}{2}J_3 J_2^{-5/2}\{s\}\right)}_{\{\beta\}}, \tag{50}$$

and

$$\{J_{3,\sigma}\} = \{s_2 s_3 \quad s_1 s_3 \quad s_1 s_2\}^T + \frac{J_2}{3}\{1\}. \tag{51}$$

When the return is to the extension meridian ($\theta = -\pi/6$), (50) is indeterminate. Here l'Hôpital's rule is used to construct the derivative

$$\{\bar{\rho}_{,\sigma}\} = \frac{\rho}{2\sqrt{6}}[\beta_{,\sigma}]\{1 \quad -1 \quad 0\}^T, \tag{52}$$

where the derivative of $\{\beta\}$ (see Eq. (50)) with respect to $\{\sigma\}$ is given by Eq. (61). The second derivative of f with respect to $\{\sigma\}$ is given by

$$[f_{,\sigma\sigma}] = \alpha[\bar{\rho}_{,\sigma\sigma}] - [\eta_{,\sigma\sigma}], \tag{53}$$

where

$$[\eta_{,\sigma\sigma}] = \frac{[\rho_{,\sigma\sigma}]}{\xi} - \frac{\{\rho_{,\sigma}\}\{\xi_{,\sigma}\}^T}{\xi^2} - \frac{\{\xi_{,\sigma}\}\{\rho_{,\sigma}\}^T}{\xi^2} + \frac{\rho\{\xi_{,\sigma}\}\{\xi^2_{,\sigma}\}^T}{\xi^4} \tag{54}$$

and

$$\left\{\xi^2_{,\sigma}\right\} = \frac{2\xi}{\sqrt{3}}\{1\}, \quad [\rho_{,\sigma\sigma}] = \frac{\rho[J_{2,\sigma\sigma}]-\{\rho_{,\sigma}\}\{s\}^T}{\rho^2}, \quad [J_{2,\sigma\sigma}] = \frac{1}{3}(3[I]-\{1\}\{1\}^T). \quad (55)$$

The second derivative of $\overline{\rho}$ with respect to $\{\sigma\}$ is given by

$$[\overline{\rho}_{,\sigma\sigma}] = \{\overline{\rho}_{,\sigma\overline{\rho}}\}\{\overline{\rho}_{,\sigma}\}^T + \{\overline{\rho}_{,\sigma\phi}\}\{\phi_{,\sigma}\}^T + \overline{\rho}_{,\sigma\phi_{,\sigma}}[\phi_{,\sigma\sigma}], \quad (56)$$

where

$$\left\{\overline{\rho}_{,\sigma\overline{\rho}}\right\} = -\frac{\overline{ar}\sin\phi}{\overline{\rho}^2}\{\phi_{,\sigma}\}, \quad \left\{\overline{\rho}_{,\sigma\phi}\right\} = \frac{\overline{ar}\cos\phi}{\overline{\rho}}\{\phi_{,\sigma}\}, \quad (57)$$

$$\overline{\rho}_{,\sigma\phi_{,\sigma}} = \frac{\overline{ar}\sin\phi}{\overline{\rho}}.$$

The second derivative of ϕ with respect to $\{\sigma\}$ is given by

$$[\phi_{,\sigma\sigma}] = \{\phi_{,\sigma\theta}\}\{\theta_{,\sigma}\}^T + \phi_{,\theta}[\theta_{,\sigma\sigma}], \quad (58)$$

where

$$\{\phi_{,\sigma\theta}\} = \frac{\overline{a}}{\overline{r}}\left(\frac{S\overline{r}^2\left(1-(S\overline{a}/\overline{r})^2\right)^2-\overline{a}^2SC^2}{\overline{r}^2(1-(S\overline{a}/\overline{r})^2)\sqrt{1-(S\overline{a}/\overline{r})^2}}\right)\{\theta_{,\sigma}\}, \quad (59)$$

$C = \cos(5\pi/6-\theta)$ and $S = \sin(5\pi/6-\theta)$. The second derivative of the Lode angle, θ, with respect to $\{\sigma\}$ is given by

$$[\theta_{,\sigma\sigma}] = 3\tan(3\theta)\{\theta_{,\sigma}\}\{\theta_{,\sigma}\}^T - \frac{\sqrt{3}}{2\cos(3\theta)}[\beta_{,\sigma}], \quad (60)$$

where the derivative of $\{\beta\}$ with respect to $\{\sigma\}$ is given by

$$[\beta_{,\sigma}] = -\frac{3}{2}J_2^{-5/2}\left(\{s\}\{J_{3,\sigma}\}^T + \{J_{3,\sigma}\}\{s\}^T + J_3[J_{2,\sigma\sigma}]\right) \quad (61)$$
$$+ J_2^{-3/2}[J_{3,\sigma\sigma}] + \frac{15}{4}J_3J_2^{-7/2}\{s\}\{s\}^T,$$

and

$$[J_{3,\sigma\sigma}] = \frac{2}{3}\begin{bmatrix} s_1 & s_3 & s_2 \\ s_3 & s_2 & s_1 \\ s_2 & s_1 & s_3 \end{bmatrix}. \quad (62)$$

We now have the all derivatives required for Eq. (44). These have been determined in principal stress form. The full sixth-order consistent tangent is given by

$$[D^{alg}] = \begin{bmatrix} \left[\hat{D}^{alg}\right] & [0] \\ [0] & (E/2(1+v))[\overline{Q}] \end{bmatrix}, \quad (63)$$

where $[\hat{D}^{alg}]$ is the consistent tangent in principal form, from Eq. (44), and $[\overline{Q}]$ is given by [4]

$$[\overline{Q}] = \begin{bmatrix} \dfrac{\sigma_1-\sigma_2}{\sigma_{t_1}-\sigma_{t_2}} & 0 & 0 \\ 0 & \dfrac{\sigma_2-\sigma_3}{\sigma_{t_2}-\sigma_{t_3}} & 0 \\ 0 & 0 & \dfrac{\sigma_1-\sigma_3}{\sigma_{t_1}-\sigma_{t_3}} \end{bmatrix}. \quad (64)$$

3.5. Stress return error analysis

The accuracy of the stress return algorithm was assessed for $1 \leq \rho_t/(\alpha\overline{\rho}(\theta_t)\xi_t) \leq 6$ and $-\pi/6 \leq \theta_t \leq \pi/6$. A Young's modulus of 100 MPa and a Poisson's ratio of 0.2 were used for the material's elastic properties. $\alpha = -0.25$ and $\overline{\rho}_e = 0.80$ define the MR cone. A hydrostatic pressure of $\xi_t = -1$ MPa was used for all of the elastic trial stresses. In this analysis, the starting stress state was positioned on the yield surface at the shear meridian ($\theta = 0$). The constitutive model was then subjected to an elastic strain increment corresponding to the elastic trial stress state, see Fig. 7(B). The return stress from this single strain increment was compared with the solution obtained by splitting the strain increment into 10,000 sub-increments.

The following error measure was used to assess the accuracy of the stress return algorithm

$$e = \frac{\sqrt{\{\{\sigma_{cp}\}-\{\sigma_e\}\}^T\{\{\sigma_{cp}\}-\{\sigma_e\}\}}}{\sqrt{\{\sigma_e\}^T\{\sigma_e\}}}, \quad (65)$$

where $\{\sigma_e\}$ is the "exact" stress return corresponding to the sub-incremented solution and $\{\sigma_{cp}\}$ is the one-step analytical return. A
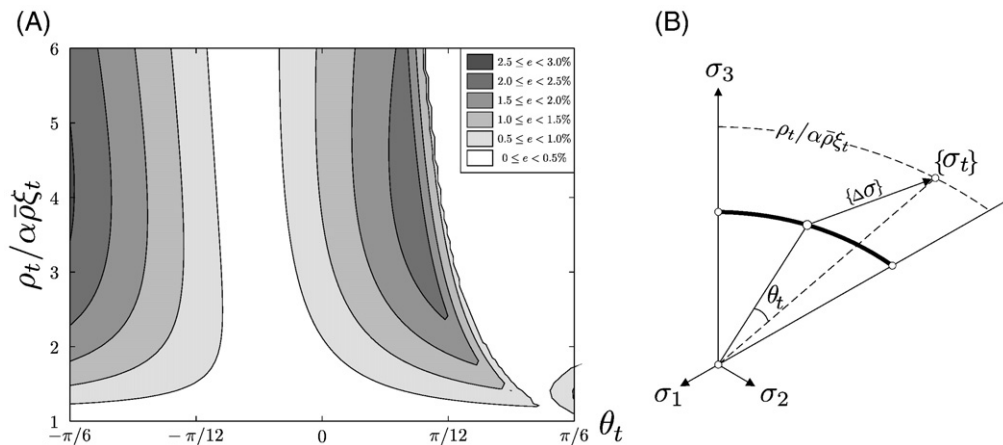

Fig. 7. (A) Errors associated with the single-step analytical backward Euler stress return. (B) Geometric interpretation of the error analysis.
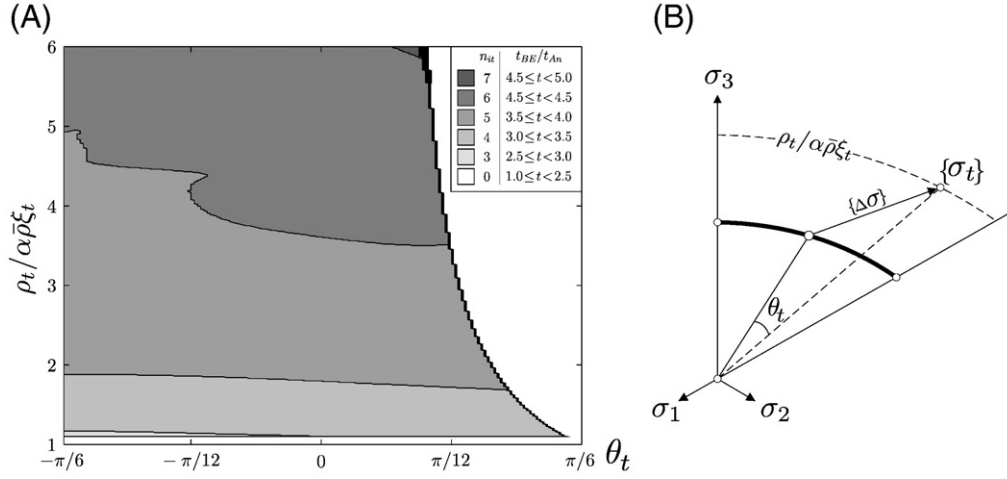
Fig. 8. (A) Run time comparison between conventional iterative backward Euler and the single-step analytical backward Euler stress return. (B) Geometric interpretation of the run time analysis.

stress iso-error map is given in Fig. 7(A). This analysis revealed a maximum error of 2.56%, corresponding to a trial stress on the extension meridian ($\theta = -\pi/6$) at $\rho_t/(\alpha\overline{\rho}\xi_t) = 4.1$. Zero error appears along the locus $\theta_t = 0$, $\rho_t/(\alpha\overline{\rho}\xi_t) = 1$ to $\theta_t \to -0.2160$, $\rho_t/(\alpha\overline{\rho}\xi_t) \to \infty$. Much of the trial area has an error of less than 0.5%. Larger errors are associated with trial stresses near the extension meridian and in the vicinity of the compression meridian return region. These are due to the increased tangential component of the trial stress increment. The non-smooth (stepped) region close to $\theta_t = \pi/12$ is a consequence of the finite grid size either side of the return region B–C boundary.

4. Run time analysis

The run time of the single-step analytical BE return is compared with a conventional iterative BE stress return in Fig. 8. The analysis considered trial stresses between $1 \leq \rho_t/(\alpha\overline{\rho}\xi_t) \leq 6$ and $-\pi/6 \leq \theta_t \leq \pi/6$. A Young's modulus of 100 MPa and a Poisson's ratio of 0.2 were again used for the material's elastic properties. Similarly, $\alpha = -0.25$ and $\overline{\rho}_e = 0.8$ define the MR cone and a hydrostatic pressure of $\xi_t = -1$ MPa was used for all of the elastic trial stresses. The constitutive model was then subjected to a strain increment corresponding to the

elastic trial stress state, see Fig. 8(B). When returning to the corner or the apex, both the approaches (analytical and numerical BE) use the same single-step return discussed in the preceding sections. However, when returning onto the non-planar surface, the conventional (numerical) BE method requires multiple local iterations to obtain convergence. The number of iterations and the ratio of the numerical to analytical BE run times are presented in Fig. 8(A). The analytical return demonstrates a 2.5–5.0 times speed-up over the iterative numerical method. The increase in time required for the iterative approach is due, in part, to repeatedly calculating the first and second derivatives of the yield function with respect to stress.

5. Finite-element performance

5.1. Single element test

A simple small-strain finite-element analysis was first undertaken to assess the constitutive model's performance within a general purpose 3D code. A single unit-cube 8-noded hexahedral element constrained on its lower horizontal, and two vertical, faces (see Fig. 9 (A)) was loaded under hydrostatic compression to -1 MPa in a single
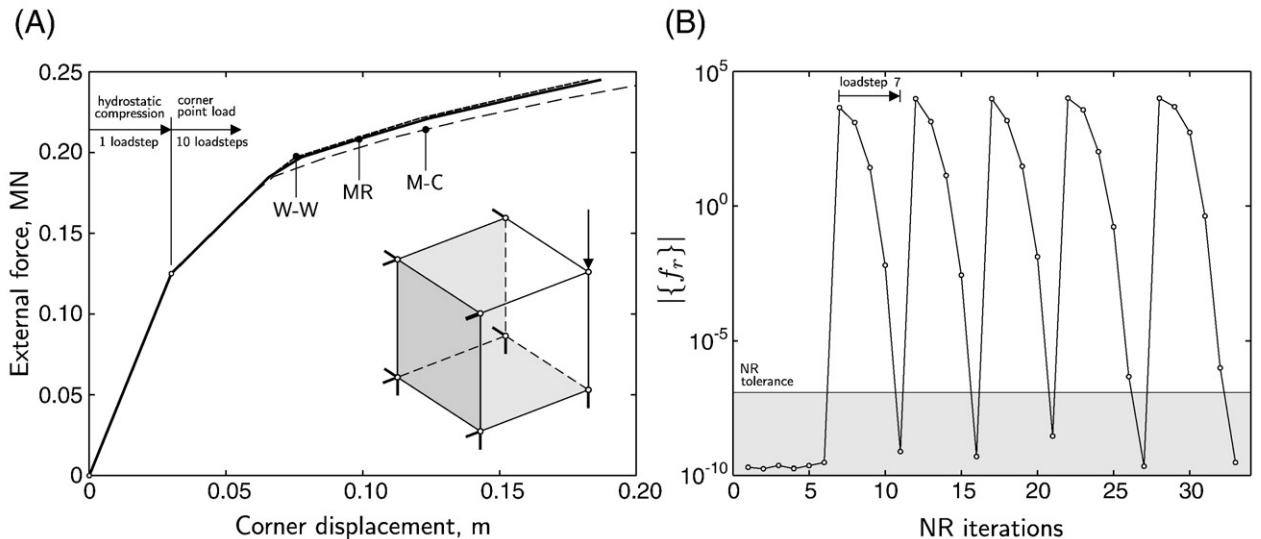

Fig. 9. (A) Force–displacement. (B) Convergence results for the single 3D finite-element simulation.

Table 1
Pseudo code for the modified Reuleaux stress return algorithm. The tolerance (tol) in steps (d) and (e) is typically set to 1×10^{-12}.

1. Input: $\{\varepsilon_t^e\}$, υ, E, α and $\bar{\rho}_e$
   (a) Transform the trial elastic strain $\{\varepsilon_t^e\}$ into principal strain form (that is, find the eigenvalues and associated eigenvectors).
   (b) Calculate the principal trial elastic stress $\{\sigma_t\} = [\hat{C}^e]^{-1}\{\varepsilon_t^e\}$.
   (c) Determine the value of the yield function f at the trial state (Eq. (6))
   (d) If $f <$ tol and $^c\xi_t <$ tol
      • Elastic response, $\{\sigma_{cp}\} = \{\sigma_t\}$
      • $[D^{alg}] = [C^e]^{-1}$
   (e) Else
      • Transform into energy-mapped space, $^c\xi_t$, $^c\rho_t$ using Eq. (14) and form $\{\varsigma_t\}$ using the Haigh–Westergaard solution Eq. (24).
      • Determine the value of the apex yield function f_a Eq. (17).
      • If $f_a <$ tol and $^c\xi_t > $ tol
         – Apex return, $\{\sigma_{cp}\} = \{0\}$ Eq. (16).
         – $[D^{alg}] = [0]$ Eq. (18).
      • Else if $\phi_t \geq \phi_{cr}$ Eq. (19)
         – Line return, $\theta_{cp} = \pi/6$.
         – Solve for $^c\xi_{cp}$ Eq. (23), $^c\rho_{cp} = {}^c\alpha\,^c\xi_{cp}$ where $^c\alpha$ is given by Eq. (15).
         – Transform the Haigh–Westergaard coordinates back to conventional stress space.
         – Calculate $\{\sigma_{cp}\}$ from the Haigh–Westergaard solution Eq. (24) and $[D^{alg}]$ from Eq. (33).
      • Else
         – Surface return
         – Solve the quartic Eq. (38) for $^c\xi_{cp}$.
         – Calculate θ_{cp} from Eq. (41) and $^c\rho_{cp}$ from Eq. (2).
         – Transform the Haigh–Westergaard coordinates back to conventional stress space.
         – Calculate $\{\sigma_{cp}\}$ from the Haigh–Westergaard solution Eq. (24) and $[D^{alg}]$ from Eq. (63).
   (f) Transform the principal measures back to generalised space using the eigenvectors from the trial elastic strain.
2. Output: $\{\sigma_{cp}\}$, $\{\varepsilon_{cp}^e\}$ and $[D^{alg}]$.

(elastic) loadstep. Subsequently, a vertical point load of -0.12 MN was applied to the element's unconstrained top corner, via 10 equal loadsteps. A Young's modulus of 100 MPa and a Poisson's ratio of 0.2 were again used for the material's elastic properties. $\alpha = -0.25$ and $\bar{\rho}_e = 0.85$ were adopted to define the MR, M–C and W–W cones. The load–displacement curves for the unconstrained corner in the vertical direction are shown in Fig. 9(A). Fig. 9(B) illustrates the MR global convergence properties of the N–R iterations for each of the 11 loadsteps. Loadsteps 1–6 resulted in an elastic material response, whereas for loadsteps 7–11 the material behaviour was elasto-plastic. The latter demonstrate the asymptotic quadratic convergence of the N–R procedure. The following measure of (residual) out of balance force

$$|\{f_r\}| = \sqrt{\{\{f_{\text{ext}}\} - \{f_{\text{int}}\}\}^T \{\{f_{\text{ext}}\} - \{f_{\text{int}}\}\}} \qquad (66)$$

was used to assess convergence, where $\{f_{\text{ext}}\}$ and $\{f_{\text{int}}\}$ are the external and internal forces, respectively. $|\{f_r\}|$ for loadsteps 7–11 are given in Table 2. The tolerance in steps (d) and (e) of the algorithm in Table 1 was set to 1×10^{-12}, which corresponds to a N–R absolute tolerance of 1.2×10^{-7} N.

Table 2
Residual out of balance force $|\{f_r\}|$ values for the finite-element simulation. Normalised residual out of balance force.

Iteration	Loadstep				
	7	8	9	10	11
1	4.5576e+03	9.818e+03	9.7542e+03	1.0232e+04	1.0170e+04
2	1.2707e+03	1.3712e+03	1.4912e+03	3.7705e+03	4.9317e+03
3	2.6853e+01	1.3767e+01	3.0343e+01	1.0539e+02	5.4714e+02
4	6.4122e−03	2.7541e−03	1.3201e−02	1.7086e−01	4.2900e−01
5	7.7098e−10	5.0493e−10	2.8944e−09	4.6539e−07	9.8050e−07
6	–	–	–	21973e−10	3.0211e−10

Table 3
Single 3D finite-element run time comparison.

	M–C	MR$_{An}$	MR$_{Num}$	W–W
Σ(NR$_{it}$)	36	33	33	32
max(NR$_{it}$)	6	6	6	6
$t/t_{\text{M–C}}$	1	1.046	1.387	1.305

The results obtained from the three constitutive models are qualitatively similar, with the W–W and MR cones producing marginally stiffer responses when compared against the M–C simulation. A run time comparison for the single element test is presented in Table 3, where $\sum$(NR$_{it}$) is the total number of global N–R iterations, max (NR$_{it}$) is the maximum number of iterations in any loadstep and $t/t_{\text{M–C}}$ is the run time normalised with respect to the M–C run time. The analytical BE MR approach (MR$_{An}$) was just 4.6% slower than the (over-simplified) M–C scheme. The analytical BE MR algorithm gave a 34.1% speed gain over the iterative BE MR approach (MR$_{Num}$). More significantly, the Willam–Warnke (W–W) formulation, which produced similar results to the MR cone, required a 25.9% increase in the run time.

5.2. Rigid strip footing analysis

A plane-strain incremental finite-element analysis of a 1 m wide rigid strip footing bearing onto a weightless soil was performed to assess the MR model's performance within a larger finite-element problem. Due to symmetry, only one half of the problem was considered. The same finite-element discretisation as presented in [6] was used, to allow comparisons to be made. The mesh had a depth and width of 5 m (Fig. 10). 135 eight-noded quadrilaterals, with reduced four-point quadrature, modelled the problem. The footing was assumed to be rigid and smooth with an imposed vertical displacement, u. Identical material properties as used in [6] were adopted here. These were: a Young's modulus of 10 GPa, Poisson's ratio of 0.48, cohesion, c, of 490 kPa, friction angle of 20° and $\bar{\rho}_e = 0.8$
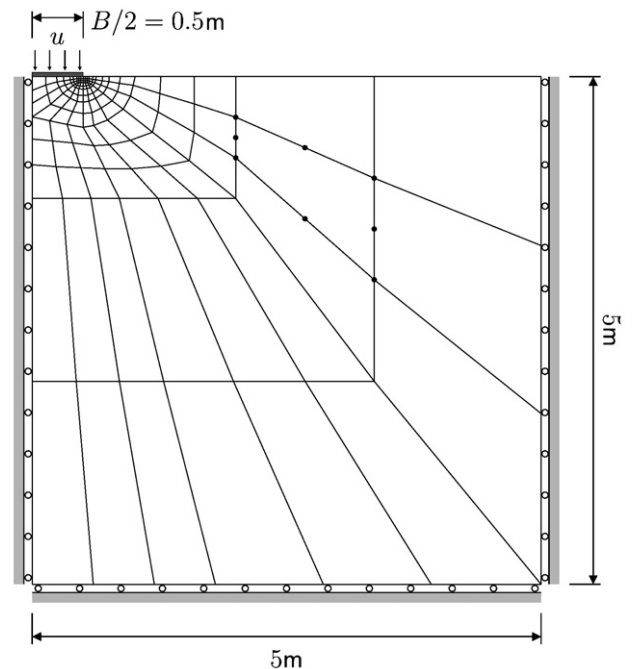

Fig. 10. Rigid strip footing plane-strain finite-element discretisation.

(to coincide with $\overline{\rho}_e$ for M–C). The material constants were common for the M–C, W–W and MR analyses.

Fig. 11 presents the normalised pressure–displacement results for the three constitutive models. The M–C simulation gave a close agreement with the results presented by de Souza Neto et al. [6]. The normalised peak pressure approached the theoretical Prandtl solution ($p/c = 14.8$) to within 1.1%. Results for the MR cone using $\overline{\rho}_e = 0.51$ and $\overline{\rho}_e = 0.99$ demonstrate the model's ability to provide solutions spanning between those provided by the M–C and D–P cones. With $\overline{\rho}_e = 0.8$ the MR cone produced a stiffer response when compared against the M–C solution. The limit load tended to $p/c = 19.36$. Results obtained from the W–W cone were quite similar; approaching a limit of $p/c = 20.69$.

Table 4 gives run time comparisons for the three constitutive models at a vertical displacement of *2 mm*. n_{Gp} is the number of Gauss points which underwent plastic deformation by the end of the analysis. t/NR_{it} gives the run time per global N–R iteration, whereas the ratio $(tNR_{it})/(t_{M-C}NR_{it}^{M-C})$ gives this time normalised with respect to the M–C iteration time. The W–W model required a 28.7% longer run time than the MR solution. The computational savings would be higher if a more efficient linear solver were used. Here the finite-element algorithm was coded in MATLAB m-script; using the backslash operator to solve the linear system. While the benefits of the MR formulation are already evident, a tuned pre-conditioned element-by-element Krylov solver [14], for example, would probably have reduced the CPU time associated with the linear solve, relative to the time spend on elasto-plastic stress integration. If this were the case, then the overall run time advantage of the MR model would be even greater.

6. Conclusion

The Drucker–Prager and Mohr–Coulomb models are amongst the most widely used simple pressure-sensitive perfect plasticity formulations in geomechanics. However, they fail to incorporate both the Lode angle and intermediate principal stress dependency typically seen in geomaterials. This omission has been shown by others to lead to errors in finite-element simulations [2]. Many constitutive models

Table 4
Rigid strip footing plane-strain finite-element run time comparison.

	M–C	MR$_{An}$	W–W
$\Sigma(NR_{it})$	6741	6075	6378
$\max(NR_{it})$	12	10	11
n_{Gp}	473	470	470
t/t_{M-C}	1	0.921	1.239
$\dfrac{tNR_{it}^{M-C}}{t_{M-C}NR_{it}}$	1	1.022	1.309

now include such dependencies, but the algebraic expressions describing those formulations are relatively complex. This necessitates iterative numerical schemes to integrate the stresses. This can present a significant computational burden when undertaking detailed 2D and 3D analyses.

This paper presents the complete formulation for an associated perfect plasticity cone model which includes sensitivities to the Lode angle and the intermediate principal stress. It is based on a conical surface with modified Reuleaux deviatoric sections. The model allows the stresses to be integrated exactly when the previous and elastic trial stresses fall within the fan zones of the tensile apex or compression meridian (zones A and B respectively in Fig. 3). Small integration errors associated with the backward Euler scheme may be introduced when returning to the curved surface (Fig. 7). For all regions, a single-step procedure is all that is required for the backward Euler approach.

The paper has demonstrated that the model offers an attractive alternative to the Drucker–Prager and Mohr–Coulomb models. Through material point and 2D plus 3D finite-element simulations, it has been shown that the computational advantages over a W–W cone model are significant (Tables 3 and 4). The paper provides all the expressions for the consistent tangent appropriate for the three stress return regions on the yield surface. The model is simple to code (see Table 1) and will be of interest to those simulating the behaviour of geomaterials and powders, where the response is governed by frictional slip.
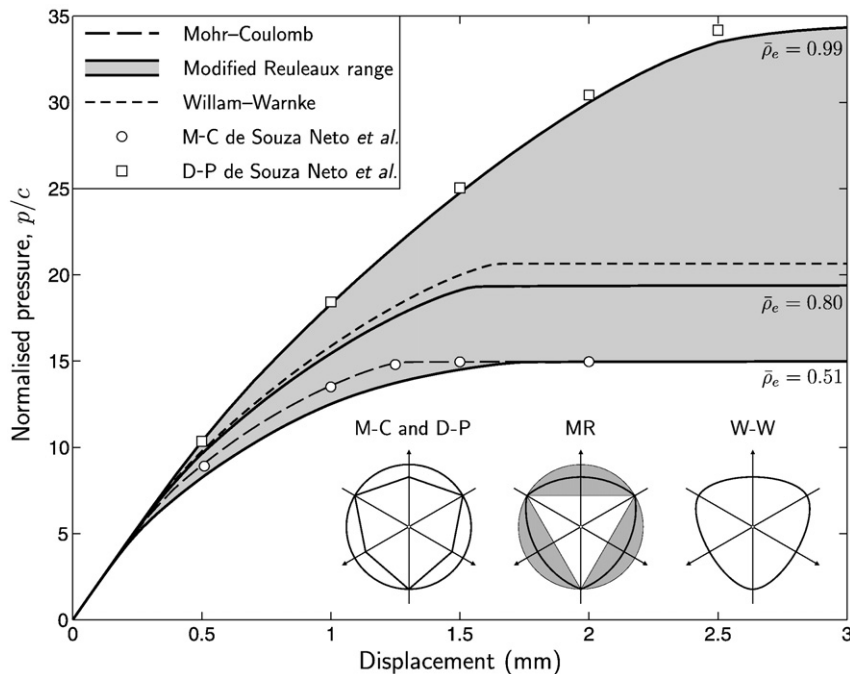

Fig. 11. Normalised pressure–displacement for the rigid strip footing plane-strain finite-element analysis.

References

[1] J.P. Bardet, Lode dependences for isotropic pressure-sensitive elastoplastic materials, ASME, J. Appl. Mech. 57 (1990) 498–506.

[2] Z. Benz, M. Wehnert, P.A. Vermeer, A Lode angle dependent formulation of the Hardening Soil model, 12th IACMAG, 2008, pp. 653–660.

[3] S.K. Bhowmik, J.H. Long, A general formulation for the cross sections of yield surfaces in octahedral planes, in: G.N. Pande, J. Middleton (Eds.), Numenta 90, 1990, pp. 795–803.

[4] J. Clausen, L. Damkilde, L. Andersen, Efficient return algorithms for associated plasticity with multiple yield planes, Int. J. Numer. Meth. Engng. 66 (2006) 1036–1059.

[5] R.S. Crouch, H. Askes, T. Li, Analytical CPP in energy-mapped stress space: application to a modified Drucker–Prager yield surface, Comput. Meth. Appl. Mech. Engrg. 198 (5–8) (2009) 853–859.

[6] E.A. de Souza Neto, D. Perić, D.R.J. Owen, Computational Methods for Plasticity: Theory and Applications, John Wiley & Sons Ltd, , 2008.

[7] D.V. Griffiths, Failure criteria interpretation based on Mohr–Coulomb friction, ASCE, J. Geotech. Engrg. 116 (6) (1990) 986–999.

[8] P.V. Lade, J.M. Duncan, Cubical triaxial tests on cohesionless soil, J. Soil Mech. Found. Div. ASCE (1973) 193–812.

[9] FC Moon, Franz Reuleaux: Contributions to 19th C. kinematics and theory of machines, Tech. report, Cornell Library Technical Reports and Papers, 2002.

[10] J. Podgorski, General failure criterion for isotropic media, ASCE, J. Engrg. Mech. 111 (2) (1985) 188–201.

[11] F. Reuleaux, The Kinematics of Machinery: Outlines of a Theory of Machines, Macmillan and Co, London, 1876.

[12] A. Sayão, Y.P. Vaid, Effect of intermediate principal stress on the deformation response of sand, Can. Geotech. J. 33 (1996) 822–828.

[13] J.C. Simo, T.J.R. Hughes, Computational Inelasticity, Springer, New York, 1998.

[14] I.M. Smith, A general purpose system for finite element analyses in parallel, Engrg. Comput. 17 (1) (2000) 75–91.

[15] M. Vrh, M. Halilovič, B. Štok, Improved explicit integration in plasticity, Int. J. Numer. Meth. Engng. 81 (2010) 910–938.

[16] K.J. Willam and E.P. Warnke, Constitutive model for the triaxial behaviour of concrete, Proceedings of the May 17–19 1974, International Association of Bridge and Structural Engineers Seminar on Concrete Structures Subjected to Triaxial Stresses, held at Bergamo Italy, 1974.

[17] M. Yu, Advances in strength theories for materials under complex stress state in the 20th century, ASME, Appl. Mech. Rev. 55 (2002) 169–218.